Precipitation kinetics of Cu-rich particles in super duplex stainless steels

Available online at www.sciencedirect.com

jmr&t Journal of Materials Research and Technology

journal homepage: www.elsevier.com/locate/jmrt

Original Article

Precipitation kinetics of Cu-rich particles in super duplex stainless steels

Vahid A. Hosseini [a,*], *Kjell Hurtig* [a], *Daniel Gonzalez* [b], *James Oliver* [c], *Nicklas Folkeson* [d], *Mattias Thuvander* [e], *Kristina Lindgren* [e], *Leif Karlsson* [a]

[a] *Department of Engineering Science, University West, SE-461 86 Trollhättan, Sweden*
[b] *Bodycote, SE-735 23 Surahammar, Sweden*
[c] *Outokumpu Stainless AB, SE-774 41 Avesta, Sweden*
[d] *ESAB AB, SE-417 55 Göteborg, Sweden*
[e] *Department of Physics, Chalmers University of Technology, SE-412 96 Gothenburg, Sweden*

ARTICLE INFO

Article history:
Received 27 July 2021
Accepted 6 October 2021
Available online 11 October 2021

Keywords:
Precipitation kinetics
Duplex stainless steels
Moving phase boundary simulation
Atom probe tomography

ABSTRACT

Complex precipitation behavior of Cu-rich particles (CRPs) was investigated and simulated in continuously cooled and quench-aged super duplex stainless steel. Atom probe tomography (APT) and scanning electron microscopy showed that slow cooling resulted in nonuniform multimodal CRP precipitation and spinodal decomposition, while in the fast cooled and quench-aged conditions, more uniform precipitation of CRPs with no visible spinodal decomposition was found. Depletion of Cu, Ni, and Mn was observed in the ferrite next to the CRPs during growth, but not during dissolution. Some evidence of Ostwald ripening was seen after slow cooling, but in the quench-aged condition, particle coalescence was observed. Large CRPs disappeared next to a ferrite–austenite phase boundary after slow cooling when Cu was depleted due to the diffusion to austenite as also predicted by moving boundary Dictra simulation. Comparing Cu depleted areas next to CRPs analyzed by APT and moving boundary Dictra simulation of CRP–ferrite showed that the effective Cu diffusion coefficient during the early-stage precipitation was about 300 times higher than the Cu diffusion coefficient in ferrite at 475 °C. Using the effective diffusion coefficient and a size-dependent interfacial energy equation, CRP size distribution was successfully predicted by the Langer–Schwartz model implemented in Thermo-Calc Prisma. Applying a short aging time and continuous cooling increased the hardness and decreased the toughness values compared to the solution annealed condition. A nonuniform distribution of Cu in ferrite, the duplex structure, and partitioning of alloying elements among different phases are factors making CRP precipitation in duplex stainless steels complex.

* Corresponding author.
E-mail address: va_hosseini@yahoo.com (V.A. Hosseini).
https://doi.org/10.1016/j.jmrt.2021.10.032

1. Introduction

Copper plays an important role to enhance the mechanical properties of steel and corrosion resistance of stainless steels [1–5]. In duplex stainless steels (DSSs), Cu is added to improve the corrosion properties; however, it also has a positive impact on slowing down the kinetics of sigma phase formation [6,7]. Copper-rich particles (CRPs) precipitate in ferrite during aging or cooling contributing to the embrittlement of DSS [6,8–10].

Precipitation of CRPs in DSS has been reported both on cooling and during isothermal aging. Depending on the composition and cooling rate, the morphology and size of CRPs are different covering small round coherent bcc particles to large incoherent fcc needles [9,11,12]. A wide range of aging temperatures has been studied in Cu-containing DSS, 290–800 °C [12–16]. Hosseini et al. [17] showed that 10 h heat treatment of 0.4 wt.% Cu super DSS (SDSS) forms CRPs in wrought plates. Lach et al. [16] reported that the presence of CRPs creates proper nucleation sites for Ni–Si–Mn particles, studied by atom probe tomography (APT).

Many studies investigated the precipitation sequence of CRPs in ferrite. The general understanding is that CRPs precipitate with the sequence of BCC → 9R → 3R → FCC between 400 and 600 °C [18]. However, other mechanisms have been also proposed for the precipitation of CRPs in ferrite [19]. In low carbon steels, for instance, Han et al. [20] reported that the precipitation of CRPs is as follows at 680 °C: nano-ordered clusters → 9R → detwinned 9R → FCC. The composition of CRPs is a controversial topic, where different characterization techniques produced different results. Despite APT studies showed high content of Fe in CRPs, some research works have considered Fe as an artifact in APT [21,22]. The general understanding, however, is that the core of CRPs has a very high Cu content, but the interface with the matrix has more Ni and Mn. This situation accommodates the interfacial energy between particle and matrix [23–25].

Simulation of CRP precipitation is of vital importance to predict the properties and lifetime of Cu-containing steel components. The experiments showed that the early stage CRP precipitation is not possible to be simulated with the known Langer–Schwartz–Kampmann–Wagner (LSKW) model, which is a standard method implemented in Thermo-Calc and MatCalc software packages [24]. The other simulation approach is called cluster dynamics (CD) where it is considered that the Cu clusters can be coupled with vacancies and have significantly faster diffusion than the Cu tracer diffusion [26,27]. This coefficient decreases with increasing number of Cu atoms in the clusters. This approach could catch the early-stage CRP precipitation [26,27]. Most recently, however, it was shown that the LSKW model can be used to simulate the CRP precipitation by defining a size dependent interfacial energy and modifying the diffusion coefficient values by two to three orders of magnitude, considering the best fit [28,29]. However, further studies are needed to find a methodology for obtaining reliable values for interfacial energy and diffusion coefficient for a specific condition.

The precipitation of CRPs demands further studies of DSS to predict possible degradation of properties in Cu-containing components during fabrication and application. The precipitation behavior next to the ferrite–austenite phase boundary in DSS is another important topic remained unstudied, as most corrosion attack and fracture occur in these regions. In DSS, the chemical composition of the precipitate–matrix interface also plays a crucial role for the corrosion resistance. Although many studies focused on the CRP chemical compositions, the chemical composition of the ferritic matrix next to CRPs has remained unmentioned in those studies. Therefore, a new perspective is required to study CRP precipitation in DSS. All these combined with thermodynamic, moving boundary, and precipitation simulations can give a comprehensive understanding of the complex behavior of CRP precipitation during cooling and aging of SDSS. Therefore, this paper is aimed at studying CRP precipitation in Cu-alloyed SDSS, subjected to hot isostatic pressing (HIP), using a combination of APT, high-resolution scanning electron microscopy (SEM), mechanical testing, as well as moving boundary and precipitation simulations. In this paper, we used APT data as an input to calculate the modified Cu diffusion in ferrite using Dictra. Then, this combined with a size-dependent interfacial energy, precipitation simulation of CRPs was performed in TC Prisma. In addition, nonuniform precipitation of CRPs after slow cooling next to the ferrite/austenite phase boundaries was successfully predicted by moving boundary Dictra simulation. Finally, experimental and simulation results were compiled to explain the complexity of CRP precipitation in DSSs and its impact on the mechanical properties.

2. Methodology

The complex precipitation of CRPs was studied using experimental work and simulations, as shown in Fig. 1, where the experiment and simulations are interconnected. SEM results were correlated with ferrite/austenite moving boundary Dictra simulation to show nonuniform precipitation of large CRPs close to the austenite phase boundary and in the bulk of the ferrite. To simulate CRP precipitation, a modified diffusion coefficient was obtained by comparing the Cu depletion area formed next to CRPs in ferrite obtained by APT analyses and CRP/ferrite moving boundary Dictra simulation at different temperatures. Then, this information combined with a size dependent interfacial energy was used to simulate the CRP precipitation using TC Prisma. The impact of different precipitation behavior was, then, correlated with mechanical testing results. The experiments and simulation are detailed in the next section.

2.1. *Experiment*

2.1.1. *Materials*

The industrially as-received powder metallurgy HIPed SDSS, known as Duplok 27, was used in this study. The nominal chemical composition of the samples is shown in Table 1. Four material conditions were studied to capture different behaviors of the CRP precipitation:

CuHIP-35: Solution heat treatment at 1070 °C and cooled down with the rate of 35 K/min.

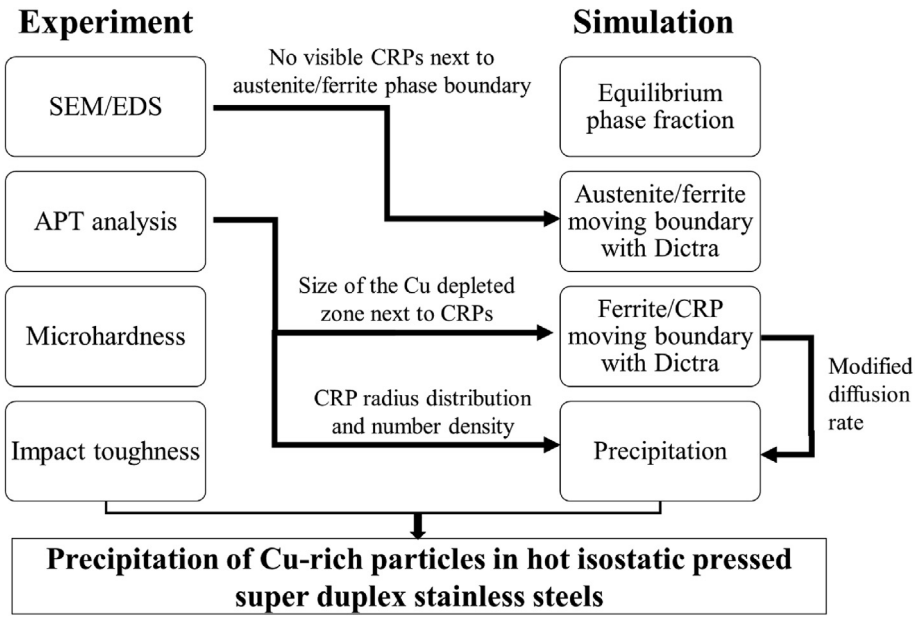

Fig. 1 – Methodology employed to study CRP precipitation in CuHIP SDSS. Interconnection between experiment and simulation to study the complex behavior of CRP precipitation.

CuHIP-100: Solution heat treatment at 1070 °C and cooled down with the rate of 100 K/min.
CuHIP-SAQ: Solution heat treated at 1070 °C for 5 min, quenched to below 300 °C and naturally air cooled to room temperature using Gleeble 3800 thermomechanical simulator.
CuHIP-SAQA475: Solution heat treated at 1070 °C for 5 min, quenched to 475 °C and held for 5 min, naturally air cooled to room temperature using Gleeble 3800 thermomechanical simulator.

2.1.2. *Microscopy*

The samples were ground and polished using 0.05 μm alumina followed by etching with Beraha etchant. The samples were studied with a Zeiss optical microscope. The ferrite fraction of five areas was measured using ImagePro software and their average was reported for each sample. The samples were repolished again followed by vibrational polishing using a colloidal silica mixture. Secondary electron mode of field emission Gemini 3 SEM equipped with energy dispersive spectroscopy (EDS) was used to study the nanosized particles visible in CuHIP-35. The chemical composition of ferrite in CuHIP-35 and CuHIP-100 was measured with EDS and the average of at least five areas were reported.

2.1.3. *Atom probe tomography*

Needles with the size of 0.3 mm × 0.3 mm were produced by cutting. The samples were then electropolished with two-step polishing of 10% H_3PO_4 acid for coarse polishing and 2% H_3PO_4 acid for fine polishing with a voltage of 19 V. APT was performed using a pulse fraction of 20%, at the set temperature of 55 K, a target evaporation rate of 0.2%, and to reconstruct the 3-dimensional atomic map a k-factor of 4.5, and evaporation field of 33 V nm^{-1} were employed using IVAS™ 3.6 (Cameca). A local electrode atom probe, LEAP 3000X HR™, equipped with a reflectron for improved mass resolution was used for the experiment.

In total, four ferrite samples were studied, two from CuHIP-35, one from CuHIP-100, and one from CuHIP-SAQA475. The reason for studying two samples for the CuHIP-35 condition was that the first sample showed significantly lower Cu than expected, not fitting with the EDS analysis. Interestingly the second one showed slightly higher Cu due to the presence of one large CRP. Therefore, we understood that, due to the nonuniform precipitation of CRPs, APT cannot give a complete overview of the CuHIP-35. Other conditions, in contrast, showed expected compositions, fitting well with thermodynamic calculations and EDS analysis.

A proximity histogram (proxigram) is a profile of the local concentrations of elements at the interface of the matrix-precipitate [30], where the location of the interface was assigned at 4 at.% Cu in all cases. Then, the average for all particles was generated for each condition. To illustrate the CRPs, isosurfaces with a minimum of 4 at.% Cu were also used.

To measure the size distribution, number density, and volume fraction of CRPs in CuHIP-SAQA475, a cluster analysis

Table 1 – The nominal chemical composition of CuHIP SDSS (UNS S32505).

C (wt.%)	Si (wt.%)	Mn (wt.%)	Cr (wt.%)	Ni (wt.%)	Mo (wt.%)	Cu (wt.%)	N (wt.%)
0.030 max	1.00 max	1.50 max	24.0–27.0	4.5–7.0	2.9–3.9	1.5–2.5	0.25–0.30

approach called maximum separation method was performed with parameters $N_{min} = 10$ and $d_{max} = 0.6$ nm. These parameters were chosen so that clusters were distinguished from random fluctuations in the matrix Cu content. The cluster radius was calculated using only Cu atoms (taking the detection efficiency of 37% into account) and it was assumed that they are coherent with the matrix. More detailed information regarding this approach may be found in Refs. [31,32].

2.1.4. *Mechanical testing*

A Shimadzu HMV-2 was used to measure the microhardness of the ferrite with an applied force of 0.01 N and an average of minimum 6 measurements for each condition is reported. Charpy impact toughness was performed at −40 °C with a Zwick Roll machine and the average of three measurements is reported for each condition.

2.2. *Multiscale simulation approach*

2.2.1. *Phase diagram*

The equilibrium phase diagram was calculated for the average nominal composition of the alloy using Thermo-Calc with the database TCFE10. All phases were considered for the calculations.

2.2.2. *Ferrite–austenite moving boundary movement simulation*

The redistribution of alloying elements compared to at the solutionizing temperature is expected to occur to the largest extent in the slowly cooled sample, as atoms have more time to diffuse during cooling. Therefore, we modeled the ferrite and austenite phase boundary using Dictra, Thermo-Calc. The model was defined with the following initial conditions:

- The total size of the system was considered as 40 μm, with 50% ferrite and 50% austenite with a planar interface. This fits well with the size of ferrite and austenite in the microstructure.
- The content of alloying elements at 1070 °C obtained from the equilibrium calculations was used for the calculations.
- Mn, Si and C were not considered in the calculations to simplify the calculations for Dictra. The chemical composition of ferrite and austenite is detailed in Table 2.
- Cooling time was 289 s from 1070 °C to 900 °C, corresponding to 35 K/min.

2.2.3. *CRP–ferrite moving boundary simulation*

This simulation approach aims at finding the size of the Cu depleted zone next to CRPs, correlating it with experimental values, and using the information for the precipitation model in 3.4. The chemical composition of the interface between CRP and ferrite was modeled using Dictra, Thermo-Calc, with the following assumptions:

- Only BCC ferrite and BCC CRP were selected in the dataset.
- A spherical model was used for the calculation with the initial ferrite size of 10 nm and a very small piece of BCC CRP.
- The chemical composition of ferrite was measured by APT and only Cu, Fe, Cr, Mo, and Ni were considered in the calculations, as more elements make the calculation of multicomponent diffusion impossible, particularly at low temperatures.
- Two temperatures of 475 °C and 570 °C were simulated. The 570 °C was chosen as it gave quite close values with the APT results.

Table 2 – The content of the alloying elements used for the calculation, obtained from the equilibrium phase fraction calculations of average composition in Table 1 without considering Mn, Si, C (wt.%).

Phase	Cr	Cu	Fe	Mo	N	Ni
Ferrite	28.9	1.1	60.7	4.7	0.06	4.3
Austenite	25.2	2.4	62.7	2.7	0.38	7.9

2.2.4. *CRP precipitation simulation*

The Langer–Schwartz–Kampmann–Wagner precipitation model was used to simulate nucleation, growth, and coarsening of CRPs. We used TC-Prisma to simulate the copper precipitation in the Cu-containing steels. More details about the model may be found in Refs. [33,34]. The main assumptions in the model were as follows:

- Same as the previous section, only BCC ferrite and BCC CRP were selected in the dataset.
- The actual chemical composition of ferrite measured by APT was used for the simulation.
- The choice of interfacial energy has been a controversial topic when comparing different studies for BCC CRP–ferritic matrix. The values have been between 0 and 0.56 J m^{-2} at 500 °C [34,35]. Although in many studies [36], and the default approach of TC-Prisma, it is considered as a constant value, interfacial energy is known to be dependent on the size of particles. Stechauner [37] considered a correcting factor of 0.6–1 depending on the particle size. Therefore, based on the literature and Thermo-Calc constant (0.46 J m^{-2} at 475 °C), we considered 0.0521*log(r*1e9) + 0.445 for particle range up to a radius of 1.5 nm, which provides the range of 0.36–0.46 J m^{-2}. This range fits very well with literature data considering the correction factor [37].
- As we did not use the cluster dynamic approach, we considered the Thermo-Calc calculated diffusion rate 300 times higher than the equilibrium at 475 °C based on the previous section. This compensates cluster mobility, but for longer times than 5 min.
- Nucleation sites were considered homogenous.

3. Experimental results

In this section, the results related to the experiment are presented. The results include microstructure and mechanical properties, the chemical composition of ferrite, precipitation of CRPs, matrix–CRP interfaces, and finally SEM studies of the ferrite/austenite interface zone. Some results in this section were used as input to develop the moving boundary and precipitation models in section 4, as shown in Fig. 1.

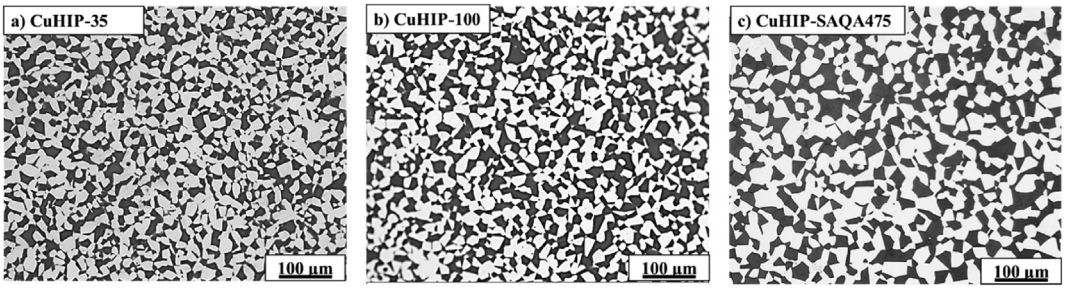

Fig. 2 – Microstructure of different CuHIP samples, where the bright phase is austenite and the dark phase is ferrite.

3.1. *Ferrite fraction and mechanical properties*

The microstructures of slowly and fast cooled as well as solution annealed-aged samples are shown in Fig. 2. The equiaxed austenite grains are present in the ferritic matrix. No traces of sigma and chi were found in the microstructure.

The samples contained equiaxed austenite grains in a ferritic matrix. The slowly cooled sample had a lower ferrite fraction and quenched samples had the lowest, as detailed in Table 3. The solution annealed sample showed some coarsening of the austenite grains. As this paper aims to study a phase transformation in ferrite, the microhardness of ferrite is shown in Table 3. The as-quenched ferrite showed the lowest hardness, but the other samples showed quite similar hardness. The impact toughness values of CuHIP-35 and CuHIP-SAQA475 are quite equal, with almost half of the CuHIP-SAQ sample. The impact toughness of CuHIP-100 was about 20 kJ higher than those for CuHIP-35 and CuHIP-SAQA475.

3.2. *Chemical composition of ferrite*

The chemical composition of ferrite, measured with APT, is detailed in Table 4. EDS analysis was also performed on CuHIP-35 and CuHIP-100. The EDS was performed due to the unexpected low Cu content in CuHIP-35-L1. In addition, APT was performed on another needle from CuHIP-35-L2, to see the possible variation in the content of alloying elements.

EDS analysis of CuHIP-100 and CuHIP-35 is quite similar with some variation in Ni and Mn content, but the Cu content was similar in both cases, meaning that on a macroscopic scale Cu was evenly distributed in the bulk of the ferrite grains. In addition, APT results of CuHIP-100 and CuHIP-SAQA475 show similar chemical composition, meaning that for these samples, the submicron chemical compositions are not much varied. CuHIP-35 showed two distinct Cu contents, but with very similar contents of other alloying elements. It should be noted that the chemical composition given includes CRPs.

3.3. *CRPs*

Different distributions of CRP precipitates were observed in the different samples. Isosurfaces of 4 at.% Cu are shown in Fig. 3 for different needles and the observations are as follows:

CuHIP-35: This sample showed two distinct appearances of CRP precipitation. L1 had very fine CRPs, but L2 had a very large CRP. The uneven distribution of CRPs, therefore, caused the difference in the composition of ferrite measured by APT (Table 4). Excluding the CRPs, both locations had very close Cu content in their ferrite matrix.
CuHIP-100: Although this sample shows a more uniform distribution of CPRs compared to CuHIP-35, some large and fine CRPs were located next to each other.
CuHIP-SAQA475: this sample showed the highest number of precipitates. As may be seen in Fig. 3, some CRPs showed coalescence.

In CuHIP-35-L1, in addition to CRP precipitation, some level of Fe and Cr separation occurred, whereas it was not seen in other samples. The isosurfaces for high Cr and high Fe regions as well as CRPs are shown in Fig. 3. As may be seen, CRPs preferred to precipitate between high Cr and high Fe regions in CuHIP-35-L1. No Fe and Cr separation was observed in other samples.

Table 3 – Ferrite microhardness and impact toughness of samples at −40 °C.

Sample	Ferrite fractions (%)	Hardness of ferrite (HV0.01)	Impact toughness (kJ)
CuHIP-35	49 ± 2	321 ± 10	50 ± 5
CuHIP-100	42 ± 2	333 ± 11	73 ± 1
CuHIP-SAQ	54 ± 1	293 ± 9	94 ± 5
CuHIP-SAQA475	54 ± 1	339 ± 27	52 ± 1

Table 4 – Chemical composition of ferrite measured by APT and EDS.

Element (at.%)	Cr	Ni	Mo	Si	Mn	Cu	Fe + some minor elements
CuHIP-100-APT	28.9	5.0	2.1	1.2	0.5	1.1	Bal.
CuHIP-100-EDS	30.4	4.7	2.1	1.3	0.8	1.2	Bal.
CuHIP-35-L1-APT	27.9	5.0	2.3	1.1	0.5	0.5	Bal.
CuHIP-35-L2-APT	27.8	4.8	2.6	1.1	0.5	2.1	Bal.
CuHIP-35-EDS	31.0	3.8	2.2	1.0	1.2	1.1	Bal.
CuHIP-SAQA475-APT	28.0	5.4	2.2	1.0	0.5	1.1	Bal.

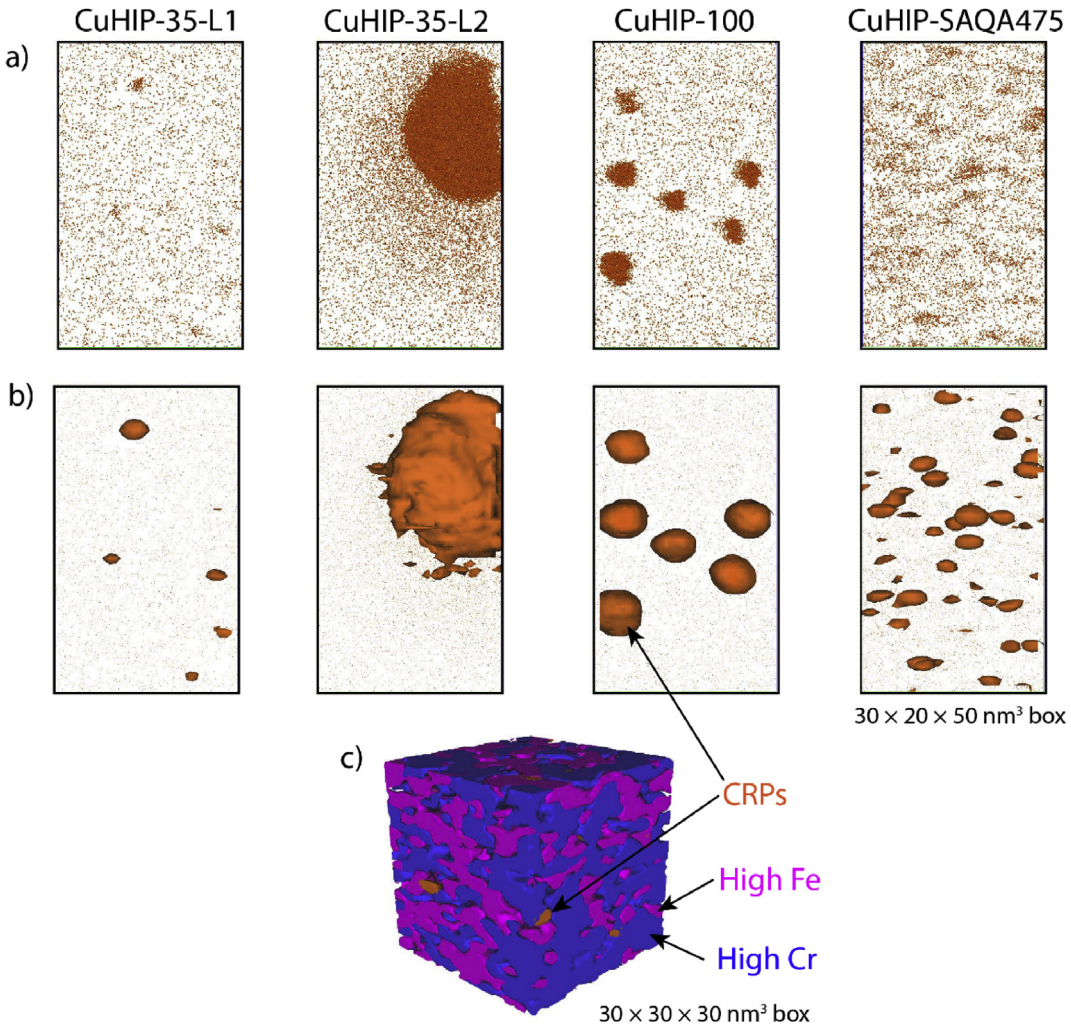

Fig. 3 – Iso-surface concentration of 4 at.% Cu for a) all Cu atoms in a volume of 20 × 30 × 50 nm^3 box are shown for all materials, b) Cu 4% isoconcentration surfaces of the same volumes are shown, where CuHIP-35-L1 with a few fine CRPs, CuHIP-35-L2 with one large CRP, CuHIP-100 with large and fine CRPs, and CuHIP-SAQA475 with a high number density of fine CRPs, where coalescence of CRPs is visible. c) a 30 × 30 × 30 nm^3 cube is shown, with Cu 2.0%, Fe 63.6% and Cr 27.7% isoconcentration surfaces; the precipitation of CRPs between high Cr and high Fe in a spinodally decomposed region of CuHIP-35-L1.

The radius (size) distribution of CRPs in CuHIP-SAQA475 is shown in Fig. 4. Using the cluster analysis method, we considered the starting of 10 detected Cu atoms as a cluster (the detection efficiency is 37%). Therefore, the size of 0.4–0.5 nm is considered as the smallest radius of CRPs. As may be seen, the particles are very fine, and the allocation of any mean diameter may result in some errors. Therefore, the radius distribution gives a more reliable view of the results. The volume fraction of CPRs is about 0.26%.

3.4. *Matrix–CRPs interface*

Proxigrams of CRPs calculated for 4 at.% isosurfaces is shown in Fig. 5. In addition to Cu, Ni is enriched in the CRPs. Inside the particle, the enrichment of Ni happened closer to the shell of the CRPs. One other interesting observation is that in all specimens, the Fe and Cr content decreased in CRPs with the same ratio.

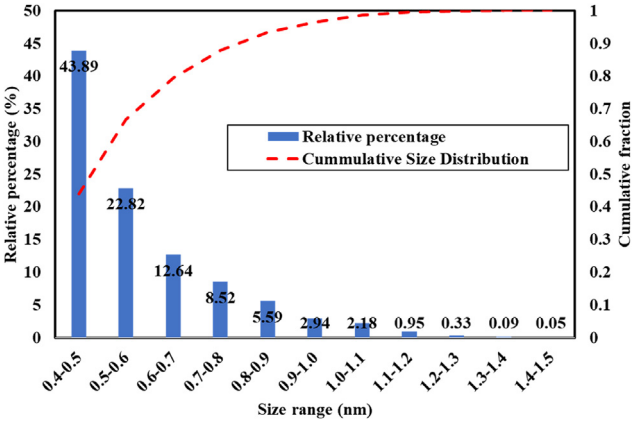

Fig. 4 – Radius distribution of detected CRPs (2112 particles) in CuHIP-SAQA475 with the assumption that they are BCC with coherent interface with ferrite.

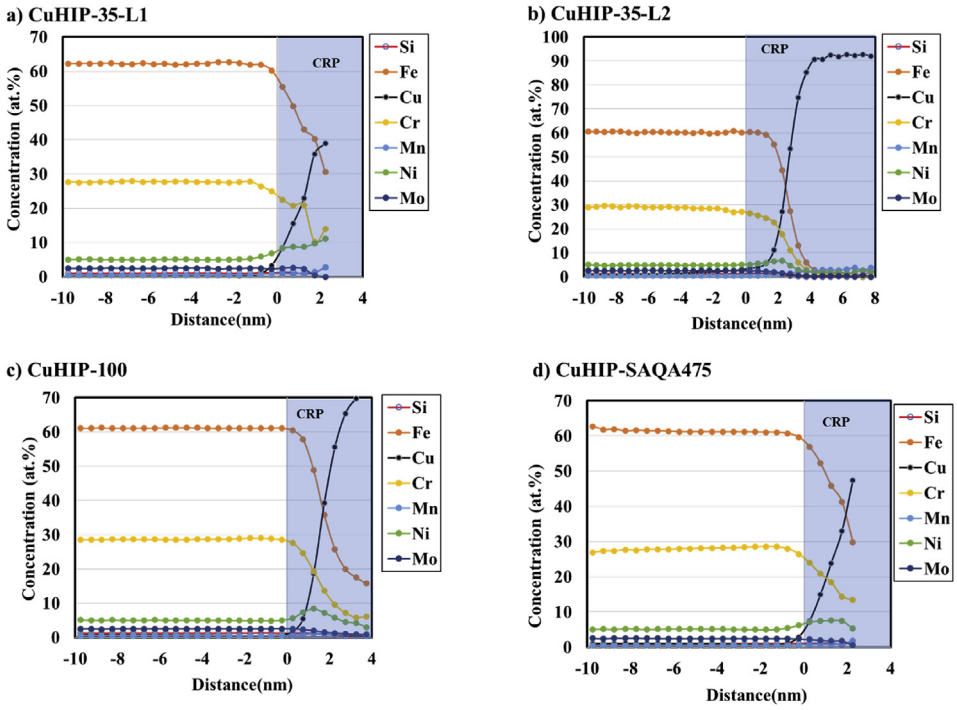

Fig. 5 – Chemical compositions at Cu precipitates and ferrite matrix in slow-cooled low Cu and fast-cooled high Cu samples. Ferrite shows a complex distribution of alloying elements where Cu, Ni, and Mn showed depletion, but Si and Cr are enriched. Mo did not show any specific partitioning trend.

A closer view of the proxigram in the interface of matrix and CRPs are shown in Fig. 6 for CuHIP-35-L1, CuHIP-100, and CuHIP-SAQA475. Cu, Ni, and Mn were interestingly depleted next to the CRPs in the ferritic matrix. In the CuHIP-SAQA475 sample, the copper content of the matrix reached 1 at.%, whereas it is 0.65 at.% in CuHIP-100 and 0.5 at.% in CuHIP-35-L1. The extent of the Cu depletion is about 9 nm in CuHIP-100, 7 nm for CuHIP-SAQA475, and 3 nm for CuHIP-35-L1.

In contrast to other samples, the big CRP in CuHIP-35-L2 showed enrichment of Cu next to the particle, where no depletion area was found (Fig. 7).

3.5. *Ferrite/austenite boundary in Cu-HIP35*

Electron backscattered SEM micrographs of the ferrite–austenite phase boundary of CuHIP-35 is shown in Fig. 8. The austenite is free from precipitates, while the ferrite contains CRPs, as expected. In addition, the ferrite/austenite phase boundary also shows some precipitates. At some locations next to the phase boundary in ferrite, no visible CRPs were found using SEM. Some CRPs are visible around 200 nm from the ferrite/austenite boundary, and their content and size increased with increasing distance from the phase boundary. SEM did not resolve the precipitation in other samples.

4. Simulation results

The results of the stepwise simulation approach are presented in this section. Equilibrium phase stability was used to calculate the formation temperature of CRPs. Ferrite–austenite moving phase boundary Dictra simulation was developed to explain the SEM analysis of nonuniform CRP precipitations close to the phase boundary. Ferrite–CRP moving phase boundary Dictra simulation correlated with proxigrams of the CuHIP-SAQA475 sample was used to study diffusion behavior of Cu in ferrite. The results were used to develop the TC Prisma simulation model with size dependent interfacial energy to simulate the CRP precipitation in CuHIP-SAQA475. The interconnection between simulation and experiment is shown in Fig. 1 in Methodology.

4.1. *Equilibrium phase stability*

The phase fraction calculation illustrated that CRPs are stable below 870 °C and its fraction increases with decreasing temperature (Fig. 9). The content of austenite increases with decreasing temperature down to 1000 °C. Other phases such as sigma, chi, and nitrides are stable below 1000 °C; however no traces of these phases were found in the samples.

4.2. *Ferrite–austenite moving phase boundary*

The results of austenite–ferrite phase transformation simulations in CuHIP35 are shown in Fig. 10. Next to the ferrite–austenite phase boundary, the depletion of Cu and Ni and enrichment of Cr and Mo occurred in ferrite. In this region, Cu drops from 1.1 wt.% to 0.9 wt.%, and Ni dropped from 4.3 wt.% to 3.3 wt.%. In contrast, Cr content can increase by about 1.5 wt.%. Slow cooling after the solution annealing, therefore, can significantly impact the content of

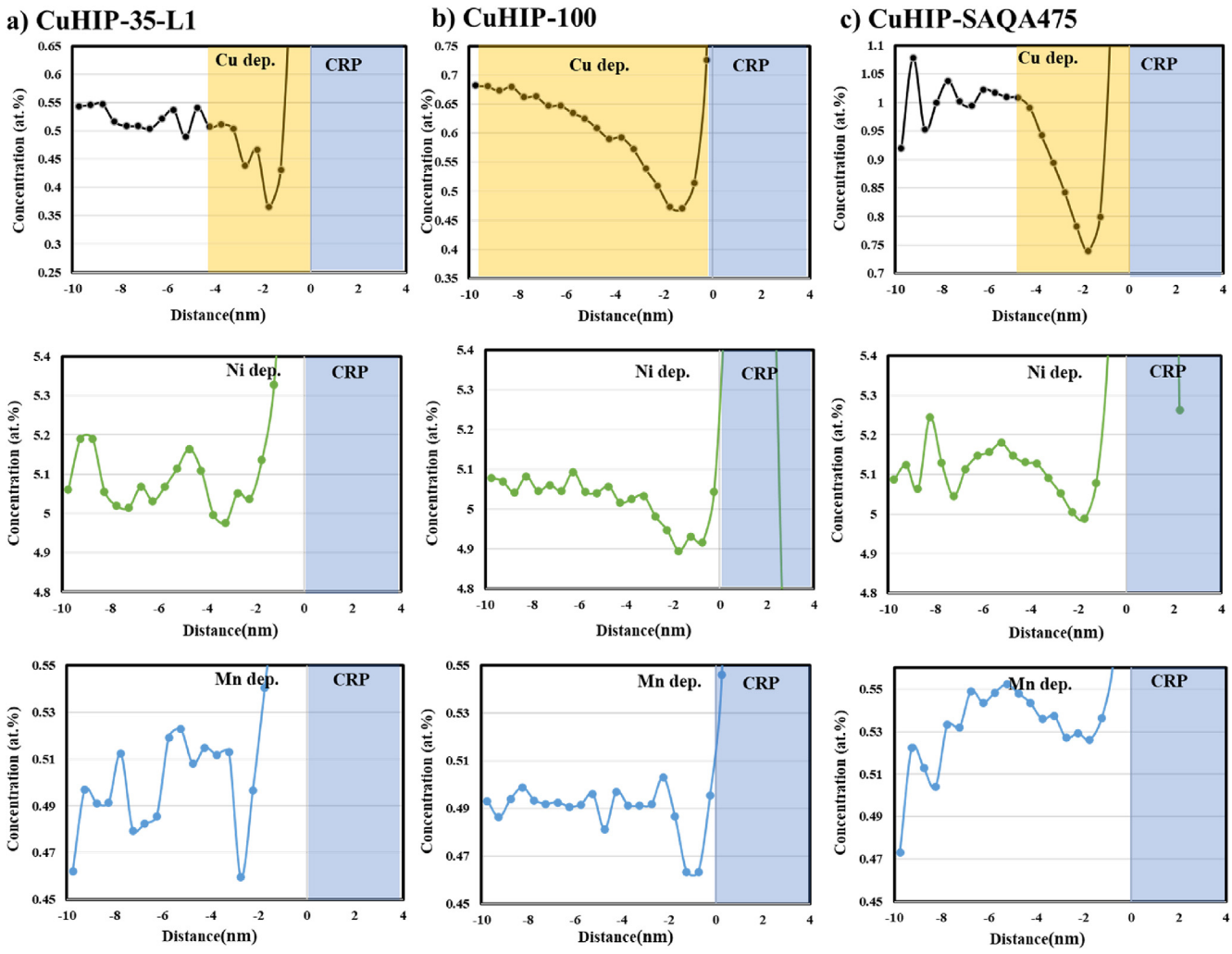

Fig. 6 – Proxigrams for CRP–ferrite boundaries. Formation of Cu, Mn, and Ni depletion regions next to CRPs. The Cu depleted region is the largest in CuHIP-100 with about 9 nm depleted region followed by CuHIP-SAQA475 with about 7 nm, and CuHIP-35-L1 with about 4 nm.

substitutional alloying elements in the ferrite–austenite phase boundary and the content of nitrogen up to the center of the ferrite grain.

4.3. *Estimation of Cu diffusion rate using moving boundary*

Phase boundary simulation is employed to estimate the depletion zone next to CRPs. As the diffusion rate is quite ambiguous when it comes to CRP precipitation, this can indicate how applicable is the extrapolated diffusion data at a certain temperature. As may be seen in Fig. 11, the Cu depletion area next to a single Cu particle is ~0.7 nm at 475 °C while ~5 nm at 570 °C (where it is a quite deep depletion). Considering these results and correlating them with the APT results of Cu depletion next to CRP size in Fig. 5, diffusion coefficient at ~570 °C gives a more logical estimation of Cu depletion area compared to 475 °C. This information is used to simulate the CRP precipitation in the next section.

4.4. *CRP precipitation at 475 °C – TC-Prisma simulation*

Considering the diffusion rate of 300 times faster than the equilibrium diffusion rates at 475 °C obtained from the previous section and radius-dependent interfacial energy of the CRPs, the results in Fig. 12 were obtained for the TC-Prisma simulation of BCC CRPs. The experimentally obtained results using APT are also added for comparison. The maximum radius of the particles, cumulative radius distribution, and volume fractions fits very well with APT results, but the simulated number density is slightly higher. It should be noted that, in simulation, we have a radius below 0.4 nm. The mean radius is about 0.6–0.7 nm in the simulation and 0.5–0.6 nm in APT results, fitting very well with each other.

5. Discussion

In this section, the precipitation behavior during cooling and aging will be discussed and the precipitation simulation

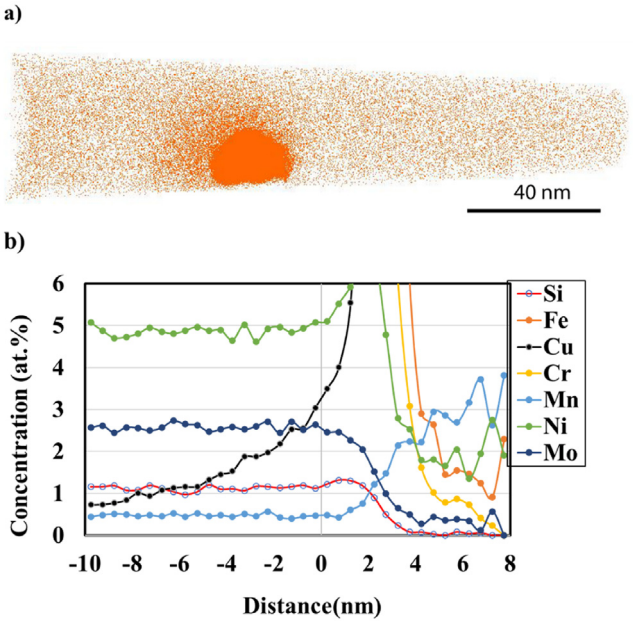

Fig. 7 – a) 3D reconstruction of Cu element and b) elemental distribution at ferrite–big CRP interface in CuHIP-35-L2, showing enrichment of Cu atoms next to the particle.

approach is evaluated, based on the methodology illustrated in Fig. 1. Then, the interfaces of ferrite–CRPs and ferrite–austenite are discussed. This gives a comprehensive overview of the complexity of CRP precipitation in Cu-containing DSS. Finally, its effect on the properties will be discussed.

5.1. *Precipitation of CRPs*

The CRP precipitation during continuous cooling and aging showed different behaviors due to the different stages of nucleation, growth, and coarsening. Their different mechanisms are summarized in Fig. 13. Three studied thermal cycles are schematically shown in Fig. 13a. The characteristics of CRPs

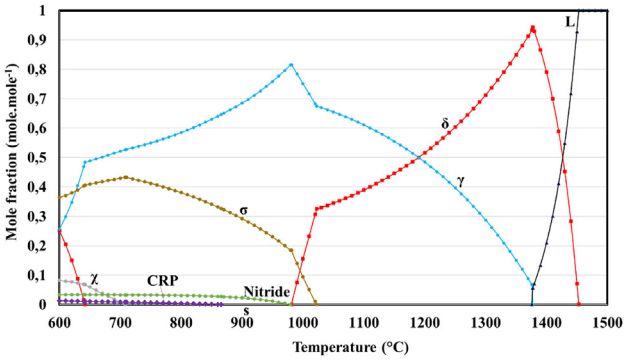

Fig. 9 – Equilibrium phase diagram of CuHIP sample.

in the ferrite matrix for these three conditions are shown in Fig. 13b. As may be seen, the CuHIP-SAQA475 sample had the highest content of Cu in the matrix followed by CuHIP-100 and CuHIP-35. The higher the content of Cu, the larger the driving force for the precipitation of CRPs will be (see Fig. 13).

5.1.1. *Evolution of microstructure during continuous cooling*

The mechanism of CRP precipitation in continuously cooled samples is shown in Fig. 13c. As described in section 4.1, CPRs are stable below 870 °C. Faster cooling increases the undercooling and the nucleation number density to some extent. Too fast cooling, in contrast, can suppress the precipitation, such as during quenching. In both conditions, the multimodal size distribution of CRPs was observed. We expect that large particles formed at higher temperatures and depleted the Cu from the matrix. Despite the reduction of Cu in ferrite by precipitation of large CRPs, further cooling reduced the solubility of Cu in the ferrite, which resulted in secondary precipitation of CRPs at lower temperatures. No trace of particle coalescence was observed in continuously cooled samples because the low nucleation number density resulted in large distances between particles allowing them to grow without coalescence. The same behavior of multimodal precipitation has been also observed during precipitation of gamma-prime in a continuously cooled superalloy [38].

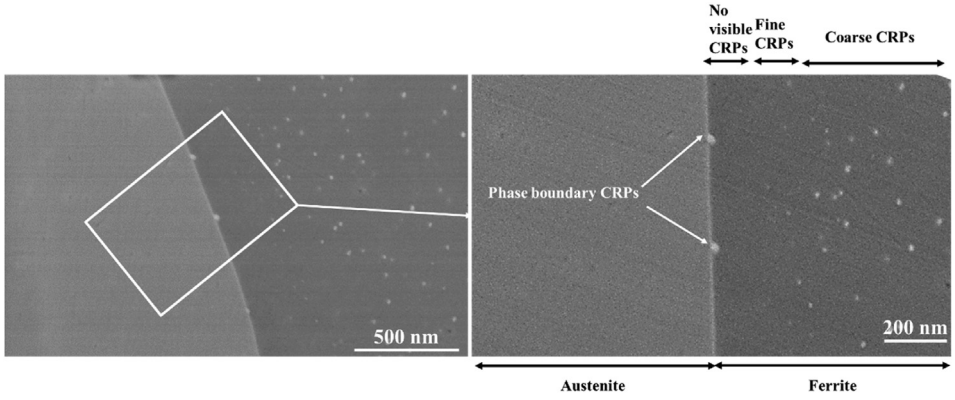

Fig. 8 – SEM micrograph of the ferrite and austenite boundary, no precipitation was observed in austenite. CRPs formed at the ferrite/austenite boundary. No visible CRPs was observed next to the phase boundary in the ferrite, continued by fine CRPs, and large CRPs.

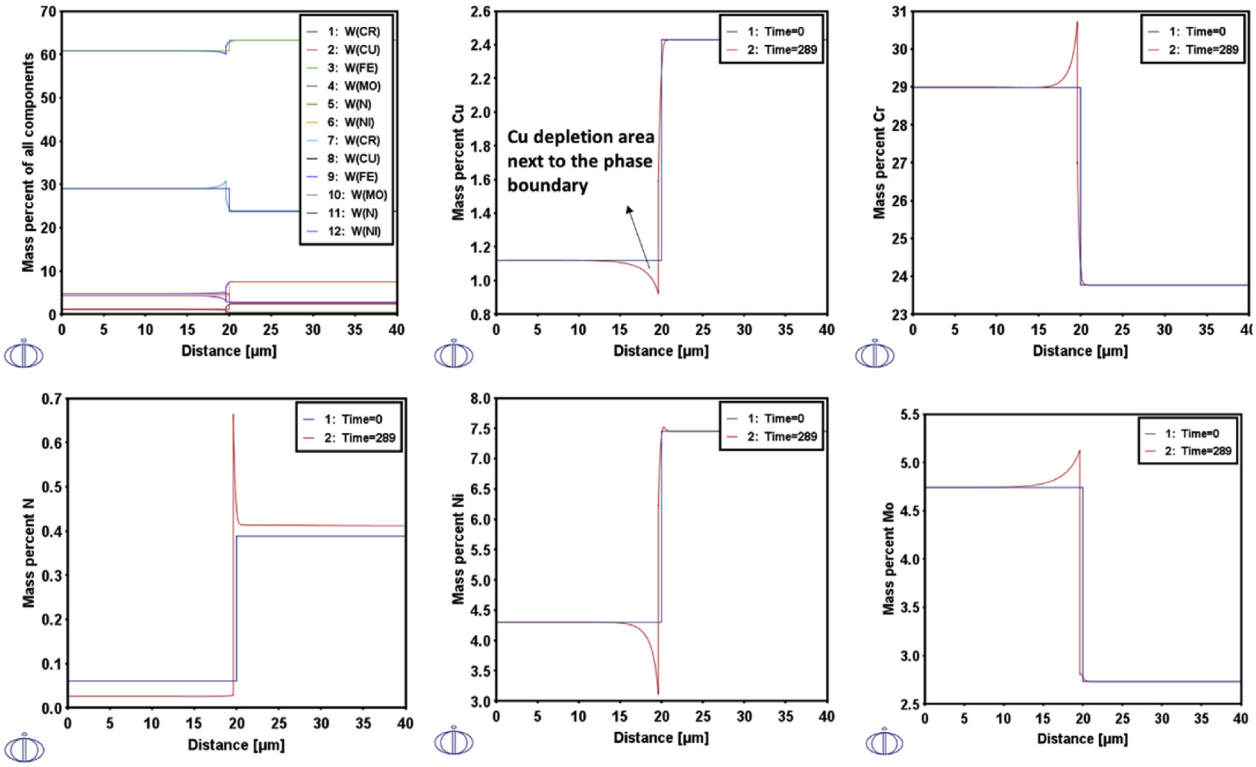

Fig. 10 – The results of ferrite–austenite moving boundary simulation after slow cooling. Formation of the Cu and Ni depletion region in ferrite next to the austenite phase boundary due to the slow cooling. Cr and Mo are enriched in the same area. N is depleted uniformly in ferrite.

In CuHIP-35-L1, fine particles formed at low temperatures due to the decreasing temperature and reduction in solubility of Cu in the ferrite. The interaction of CRPs and spinodal decomposition were quite interesting as copper preferred to nucleate between high Cr and high Fe regions. As spinodal decomposition occurs below 500 °C, this interaction also indicates that the CRPs formed at low temperatures together with spinodal decomposition. The same interaction behavior between spinodal decomposition and CRPs was also observed in aged DSS at a longer aging time of 100 h at the same aging temperature [39].

5.1.2. *Evolution of microstructure during isothermal aging*

The schematic illustration of CRP precipitation during aging for 5 min at 475 °C is shown in Fig. 13c. Very high undercooling

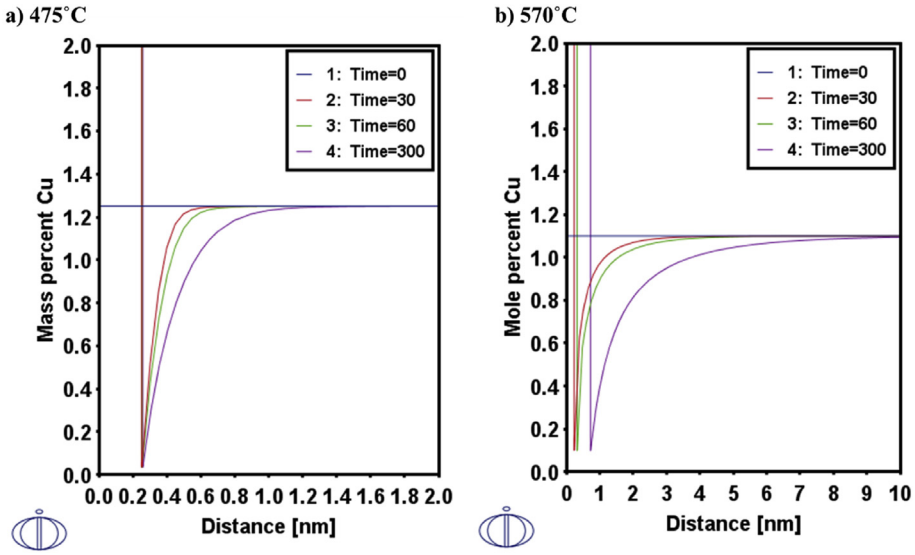

Fig. 11 – Dictra simulated distribution of alloying elements in the CRP–ferrite phase boundary formed at 475 °C and 570 °C after 5 min. It shows the maximum size of the depletion zone considering the diffusion data.

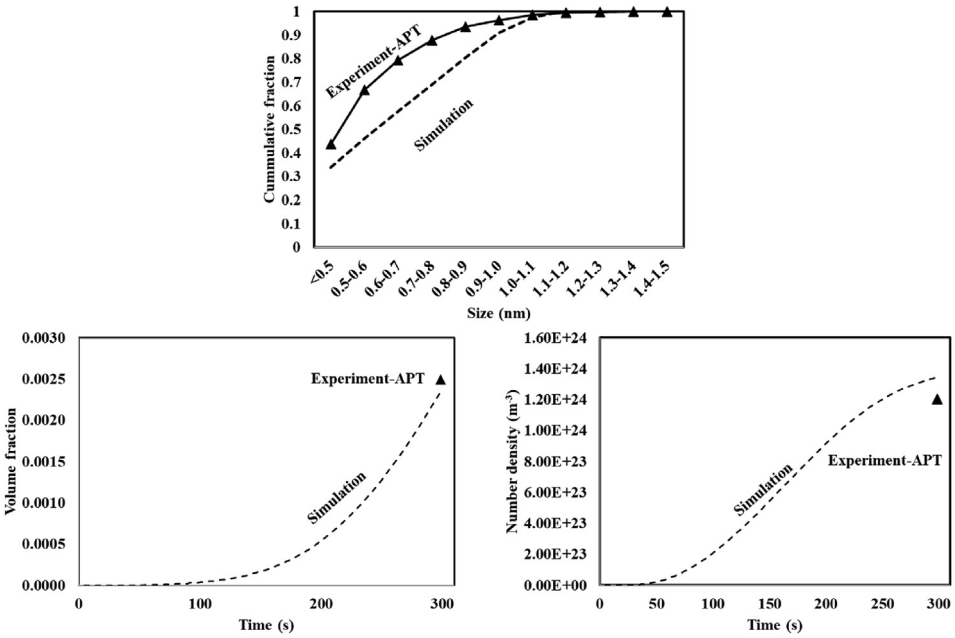

Fig. 12 – The comparison of TC-Prisma simulation and experiment for the sample aged at 475 °C. Radius distribution, number density, and volume fractions fit well with the experimental data from APT.

and supersaturated matrix of Cu resulted in precipitation of CRPs with a high number density. In this condition, fine particles form and grow. As the matrix has enough copper to allow CRPs to grow without reaching the equilibrium Cu content of ferrite, Ostwald ripening did happen during this time. Therefore, particles can grow until they join each other, known as coalescence. This behavior has been observed in standard DSSs [16].

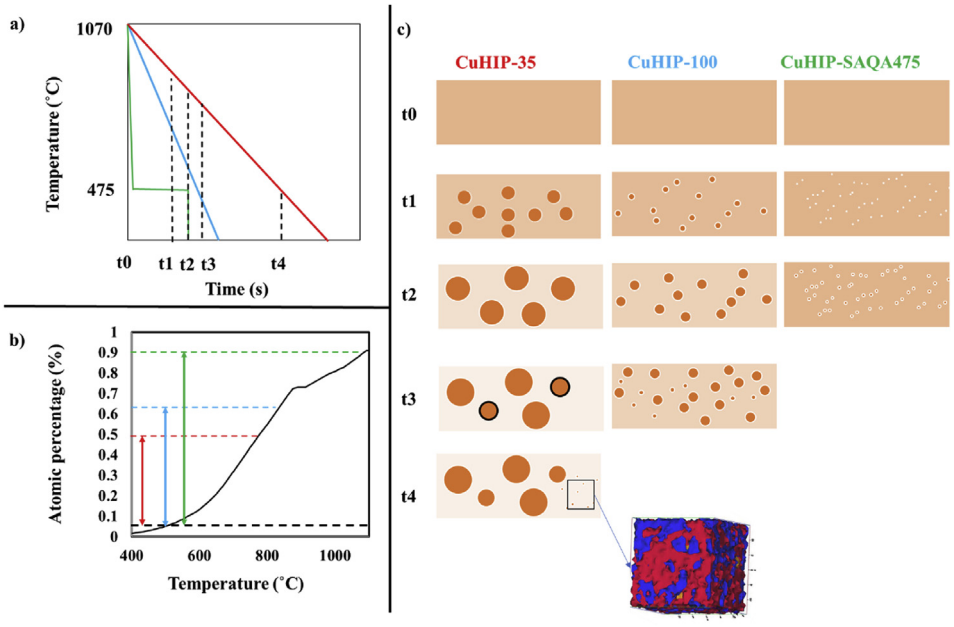

Fig. 13 – Schematic illustration of CRP precipitation in DSS processed with different thermal cycles. a) schematic illustration of thermal cycles, b) the dashed black line shows the solubility limit of Cu in ferrite at 475 °C from Thermo-Calc. The green, blue, and red lines show the Cu content of matrix for CuHIP-35, CuHIP-100, and CuHIP-SAQA475 respectively, c) precipitation behavior of three studied thermal cycles, where the particles with black circles are dissolving and with white circles are growing/coarsening. In CuHIP-35, at some point, coarsening happens with reduction of temperature via Ostwald ripening. In CuHIP-SAQA475, the coalescence of particles occurred due to the high number density and high Cu content of the matrix.

5.1.2.1. *Simulation of precipitation during aging*. The crystal structure of CRPs was assumed to be BCC, where it fits very well with the literature information, reporting that CRPs up to a radius of 1–2 nm has the BCC structure and then they transforms to other structures ending with FCC [20,40]. The chemical composition of BCC CRPs is almost 100% Cu in the Thermo-Calc database. This assumption is debatable, but in some studies, it has been shown that the copper content of CRPs is much higher than what is suggested by APT [21,22]. Dictra simulation of CRP–ferrite phase boundary showed that the monomer diffusion coefficient is inapplicable to predict the Cu depletion area formed next to CRPs. Cluster mobility is expected to play the most important role toward the diffusion of Cu atoms, where vacancies and Cu atoms pairs, resulting in faster diffusion of atoms at the early stage of precipitation. The width of the depletion area showed that Cu atoms join the nuclei faster than the known tracer Cu diffusion [26,27].

Using the data of Cu depletion region next to CPRs (Fig. 6) successfully provides the range of diffusion coefficient based on the Dictra calculations (Fig. 11) to solve the LSKW model. The size-dependent equation of interfacial energy was also successfully implemented, providing a good estimation of size distribution, volume fraction, and number density of CRPs (Fig. 12). Both experiments and simulations showed that the maximum radius of CRPs is in the range of 1.4–1.5 nm, which means that the simulation parameters fit very well to predict the early-stage radius distribution. A slightly higher number density of CRPs in simulation data is expected to be the result of the prediction of the formation of very fine CRPs (below 0.4 nm), which were not considered as clusters/particles in the APT analysis, as they could not be distinguished from random fluctuations of the Cu content in the matrix in the reconstruction.

The application of LSKW precipitation model has been the subject of some studies to simulate CRP precipitation in steels and amorphous Fe-based alloys [28,29,40–43]. In some studies [40], to fit the results, diffusion has been considered to be two to three orders of magnitude faster than that for Cu monomer diffusion. Despite this consideration, these simulations normally do not fit, for instance, volume fraction, radius, or/and number density differ from experimental results, as also stated by Cui et al. [27]. With the approach that we used in this study, we caught the early stage of BCC CRP precipitation using size-dependent interfacial energy and modified diffusion rate based on Dictra simulation. Therefore, LSKW can be also employed to model the early stages of CRP precipitation in DSS.

5.2. *Composition next to phase boundaries*

5.2.1. *CRPs–ferrite*

One of the topics that has not been covered by other studies is the matrix–CRP interface compositional variation. The ferritic matrix next to CRPs is depleted from Cu, Mn, Ni in all samples except CuHIPSlow-L2, fitting well with literature showing that Ni and Mn are enriched in the outer layer to compensate for the CRP's interfacial energy (Fig. 6). The depletion means that the CRPs are still growing. In contrast, in CuHIPSlow-L2, the absence of a depletion zone and particularly the presence of an enrichment zone are signs of dissolution of CRPs (Fig. 7). As the sample did not exceed the dissolution temperature of CRPs after cooling, we expect that this is the result of Ostwald ripening, where larger particles coarsen at the expense of dissolution of smaller particles. To the knowledge of the authors, such behavior has not been reported in the previously published data about CRPs. Precipitation of Cr-rich particles has been modeled in the aging of Fe–Cr–Al alloys, where aging at high temperatures resulted in Ostwald ripening, but at lower temperature coalescence of particles occurs [44].

5.2.2. *Ferrite–austenite in the slowly cooled sample*

Despite the very small displacement of the ferrite–austenite phase boundary toward ferrite during the slow cooling (Fig. 10), partitioning of the alloying elements can significantly differ compared to material solution annealed and quenched. Comparison of simulations and microstructure analysis clearly shows that the Cu depletion zone formed in the ferrite next to the phase boundary is responsible for the absence of large CRPs. This fits very well with the simulation of the austenite–ferrite boundary. Possibly some Cu depletion also occurred by the formation of CRPs on the ferrite and austenite phase boundaries, as they are much larger than the ones formed in the bulk.

5.3. *Mechanical properties of Cu bearing SDSS*

Mechanical properties of duplex stainless steels are influenced by different factors such as phase fraction and morphology, grain size, presence of secondary phases, and Fe and Cr phase separation [45]. Nanoscale phase separations in ferrite is the main cause for 475°C-embrittlement in DSS [46]. In the present study, solution annealed and quenched samples have the highest impact toughness values compared to other conditions (Table 3), as also reported by Smuk et al. [8]. It is attributed to the dissolution of CRPs in ferrite, resulting in easier movement of dislocations. In CuHIP-35, multimodal distribution of very large and very fine CRPs, phase boundary precipitation, nonuniform CRPs distribution, and spinodal decomposition decreased the toughness. In addition, one point that was remained unstudied in this paper was the level of spinodal decomposition close to the ferrite/austenite phase boundaries. This can also significantly contribute to reducing the toughness values but not much to increase the microhardness of the ferrite.

In CuHIP-100, a more uniform distribution of large and fine particles with no trace of visible spinodal decomposition resulted in higher impact toughness. The large CRPs are expected to have an incoherent ferrite–CRP interface. In contrast, a high number density of very fine particles in the CuHIP-SAQA475 sample with most likely coherent interfaces with ferrite can hinder the movement of dislocations, causing a drop in toughness to the same level as CuHIP-35. Therefore, the nonuniform CRP precipitation together with spinodal decomposition and phase boundary precipitation may result in the same toughness value as a uniform distribution of fine CPRs with high number density. The increase in microhardness of ferrite after 475 °C agrees with de Lima et al. studies, which was mainly attributed to precipitation of CPRs in ferrite of 3% Cu cast DSS [13]. Despite precipitation of CRPs has been also reported in austenitic stainless steels, the kinetics of

precipitation and hardness increase is very slow compared to SDSS. For instance, even 1 h heat treatment at 650 °C of super 304H and 20 min heat treatment of 316 L did not cause CRPs precipitation and hardness increase [47,48].

Smuk et al. [9] also reported the reduction of toughness in Cu-containing SDSS cooled down with the rate of 20 °C min^{-1}, however no secondary phases were found. Therefore, it is expected that nanoscale CRPs were the main reason for the toughness reduction, agreeing APT analysis in the present work. Otarola et al. [49] reported that the precipitation of CRPs was less detrimental compared to high temperature phase transformation such sigma and chi, where CRPs with higher increases in toughness resulted in less toughness drop compared to sigma phase containing samples. However, this study showed that CRPs precipitation and significant toughness loss can happens after 5 min 475 °C. Therefore, special attention must be paid to control the fabrication of Cu-bearing SDSS due to the fast degradation of properties. In addition, an increase in service temperature, even for a short time, can degrade the material properties.

6. Conclusions

The precipitation of copper-rich particles was investigated in continuously cooled (with cooling rates of 35 °C min^{-1} and 100 °C min^{-1}) and quench-aged (475 °C for 5 min) Cu-bearing HIPed super duplex stainless steel, after solution annealing at 1070 °C. The following conclusions can be drawn:

1. CRPs were observed in continuously cooled and quench-aged samples, where the aged sample had a higher number density. The slowly cooled sample showed a multimodal distribution of large and fine CRPs and spinodal decomposition. The fast cooled, slowly cooled, and quenched-aged samples showed Cu depleted regions next to the CRPs.
2. The Langer–Schwartz–Kampmann–Wagner precipitation model successfully predicted the phase fraction and radius distribution of CRPs at the early stage of precipitation (5 min at 475 °C) when introducing a modified diffusion coefficient, predicted by Dictra, and size-dependent interfacial energy.
3. Nonuniform precipitation of CRPs and local spinodal decomposition in slowly cooled material resulted in the same level of toughness and ferrite microhardness as for the as-quenched aged material with fine CRPs formed with high number density. The toughness values for these conditions were about half of those for the solution annealed quench condition at a testing temperature of −40 °C.

Declaration of Competing Interest

The authors declare that they have no known competing financial interests or personal relationships that could have appeared to influence the work reported in this paper.

Acknowledgment

The APT was performed in Chalmers Materials Analysis Lab (CMAL).

The author would like to acknowledge KK-Stiftelsen for funding of “ALWAYS project”.

REFERENCES

[1] Takaki S, Fujioka M, Aihara S, Nagataki Y, Yamashita T, Sano N, et al. Effect of copper on tensile properties and grain-refinement of steel and its relation to precipitation behavior. Mater Trans 2004;45(7):2239–44.
[2] Foehl J, Willer D, Katerbau K. Effect of copper precipitates on the toughness of low alloy steels for pressure boundary components. 2004.
[3] Takahashi J, Kawakami K, Kobayashi Y. Consideration of particle-strengthening mechanism of copper-precipitation-strengthened steels by atom probe tomography analysis. Mater Sci Eng A 2012;535:144–52.
[4] Dyja D, Stradomski Z. Quench ageing behaviour of duplex cast steel nano-scale ε-Cu particles. J Achiev Mater Manuf Eng 2007;20(1–2):435–8.
[5] Ujiro T, Satoh S, Staehle RW, Smyrl WH. Effect of alloying Cu on the corrosion resistance of stainless steels in chloride media. Corros Sci 2001;43(11):2185–200.
[6] Smuk O, Selleby M, Bergman B. The effect of copper on secondary phase precipitation in duplex stainless steel—a thermodynamic calculations approach. Z Metallkd 2005;96(8):918–23.
[7] Jeon S-H, Park I-J, Kim H-J, Kim S-T, Lee Y-K, Park Y-S. Effect of Cu on the precipitation of deleterious phases and the mechanical properties of 27Cr–7Ni hyper duplex stainless steels. Mater Trans 2014;55(6):971–7.
[8] Smuk O, Nenonen P, Hänninen H, Limatainen J. Precipitation of secondary phases in Duplok 27 duplex stainless steel with emphasis on copper effects. 2002.
[9] Smuk O, Hänninen H, Liimatainen J. Mechanical and corrosion properties of P/M-HIP super duplex stainless steel after different industrial heat treatments as used for large components. Mater Sci Technol 2004;20(5):641–4.
[10] Smuk O, Nenonen P, Hänninen H, Liimatainen J. Effects of copper on precipitation of secondary phases in duplex stainless steels. 2000.
[11] Smuk O, Nenonen P, Hänninen H, Liimatainen J. Microstructures of a powder metallurgy-hot-isostatically pressed super duplex stainless steel forming in industrial heat treatments. Metall Mater Trans A 2004;35(7):2103–9.
[12] Dyja D, Stradomski Z. Microstructural Evolution in a duplex cast steel after quench ageing process. Arch Mater Sci Eng 2007;28(9):557–64.
[13] de Lima HMLF, Tavares SSM, Araujo WS, Dille J, Malet L. Characterization of a cast duplex stainless steel with 3.0% Cu and modeling of precipitation hardening. J Mater Eng Perform 2019;28(4):2421–6.
[14] Kobayashi S, Nakai K, Ohmori Y. Isothermal decomposition of δ-ferrite in a 25Cr–7Ni–0.14 N stainless steel. Acta Mater 2001;49(11):1891–902.
[15] Soylu B, Honeycombe R. Microstructural refinement of duplex stainless steels. Mater Sci Technol 1991;7(2):137–46.

[16] Lach TG, Frazier WE, Wang J, Devaraj A, Byun TS. Precipitation-site competition in duplex stainless steels: Cu clusters vs spinodal decomposition interfaces as nucleation sites during thermal aging. Acta Mater 2020;196:456–69.
[17] Hosseini VA, Thuvander M, Wessman S, Karlsson L. Spinodal decomposition in functionally graded super duplex stainless steel and weld metal. Metall Mater Trans A 2018;49(7):2803–16.
[18] Kong HJ, Liu CT. A review on nano-scale precipitation in steels. Technologies 2018;6(1):36.
[19] Sun M, Zhang W, Liu Z, Wang G. Direct observations on the crystal structure evolution of nano Cu-precipitates in an extremely low carbon steel. Mater Lett 2017;187:49–52.
[20] Han G, Xie Z, Li Z, Lei B, Shang C, Misra R. Evolution of crystal structure of Cu precipitates in a low carbon steel. Mater Des 2017;135:92–101.
[21] Fine M, Liu J, Asta M. An unsolved mystery: the composition of bcc Cu alloy precipitates in bcc Fe and steels. Mater Sci Eng A 2007;463(1–2):271–4.
[22] Morley A, Sha G, Hirosawa S, Cerezo A, Smith G. Determining the composition of small features in atom probe: bcc Cu-rich precipitates in an Fe-rich matrix. Ultramicroscopy 2009;109(5):535–40.
[23] Liu Q, Chen Y, Li C, Gu J. Compositional variants of Cu-rich precipitate in thermally aged ferritic steel. Acta Metall Sin (Engl Lett) 2018;31(5):465–70.
[24] Wang Z, Fang X, Li H, Liu W. Atom probe tomographic characterization of nanoscale Cu-Rich precipitates in 17-4 precipitate hardened stainless steel tempered at different temperatures. Microsc Microanal 2017;23(2):340.
[25] Seko A, Nishitani SR, Tanaka I, Adachi H, Fujita EF. First-principles calculation on free energy of precipitate nucleation. Calphad 2004;28(2):173–6.
[26] Jourdan T, Soisson F, Clouet E, Barbu A. Influence of cluster mobility on Cu precipitation in α-Fe: a cluster dynamics modeling. Acta Mater 2010;58(9):3400–5.
[27] Cui S, Mamivand M, Morgan D. Simulation of Cu precipitation in Fe-Cu dilute alloys with cluster mobility. Mater Des 2020;191:108574.
[28] Golubov S, Osetsky YN, Serra A, Barashev A. The evolution of copper precipitates in binary Fe-Cu alloys during ageing and irradiation. J Nucl Mater 1995;226(1–2):252–5.
[29] Guo H, Enomoto M, Shang C. Simulation of bcc-Cu precipitation in ternary Fe-Cu-M alloys. Comput Mater Sci 2018;141:101–13.
[30] Hellman OC, Vandenbroucke JA, Rüsing J, Isheim D, Seidman DN. Analysis of three-dimensional atom-probe data by the proximity histogram. Microsc Microanal 2000;6(5):437–44.
[31] Vaumousse D, Cerezo A, Warren P. A procedure for quantification of precipitate microstructures from three-dimensional atom probe data. Ultramicroscopy 2003;95:215–21.
[32] Lindgren K, Stiller K, Efsing P, Thuvander M. On the analysis of clustering in an irradiated low alloy reactor pressure vessel steel weld. Microsc Microanal 2017;23(2):376.
[33] Jha R, Diercks DR, Chakraborti N, Stebner AP, Ciobanu CV. Interfacial energy of copper clusters in Fe-Si-B-Nb-Cu alloys. Scr Mater 2019;162:331–4.
[34] Sheng Z, Rolland MB, Zhou T, Odqvist J, Hedström P. Langer–Schwartz–Kampmann–Wagner precipitation simulations: assessment of models and materials design application for Cu precipitation in PH stainless steels. J Mater Sci 2021;56(3):2650–71.
[35] Sonderegger B, Kozeschnik E. Interfacial energy of diffuse phase boundaries in the generalized broken-bond approach. Metall Mater Trans A 2010;41(12):3262–9.
[36] Yang J, Enomoto M. Numerical simulation of copper precipitation during aging in deformed Fe-Cu alloys. ISIJ Int 2005;45(9):1335–44.
[37] Stechauner G. Simulation of precipitation in steel. Wien: von Georg Stechauner; 2017.
[38] Singh A, Nag S, Hwang J, Viswanathan G, Tiley J, Srinivasan R, et al. Influence of cooling rate on the development of multiple generations of γ′ precipitates in a commercial nickel base superalloy. Mater Charact 2011;62(9):878–86.
[39] Guo W, Garfinkel DA, Tucker JD, Haley D, Young GA, Poplawsky JD. An atom probe perspective on phase separation and precipitation in duplex stainless steels. Nanotechnology 2016;27(25):254004.
[40] Habibi-Bajguirani H, Jenkins M. High-resolution electron microscopy analysis of the structure of copper precipitates in a martensitic stainless steel of type PH 15-5. Philos Mag Lett 1996;73(4):155–62.
[41] Zhou T, Faleskog J, Babu RP, Odqvist J, Yu H, Hedström P. Exploring the relationship between the microstructure and strength of fresh and tempered martensite in a maraging stainless steel Fe–15Cr–5Ni. Mater Sci Eng A 2019;745:420–8.
[42] Zhou T, Babu RP, Odqvist J, Yu H, Hedström P. Quantitative electron microscopy and physically based modelling of Cu precipitation in precipitation-hardening martensitic stainless steel 15-5 PH. Mater Des 2018;143:141–9.
[43] Stechauner G, Kozeschnik E. Thermo-kinetic modeling of Cu precipitation in α-Fe. Acta Mater 2015;100:135–46.
[44] Chen S, Li Y, Shi S, Jin S. Quantitative phase-field simulation of composition partition and separation kinetics of nanoscale phase in Fe-Cr-Al alloy. J Nanomater 2019;2019:6862390.
[45] Gunn R. Duplex stainless steels: microstructure, properties and applications. Woodhead Publishing; 1997.
[46] Nilsson J-O. Super duplex stainless steels. Mater Sci Technol 1992;8(8):685–700.
[47] Chi C-y, Yu H-y, Dong J-x, Liu W-q, Cheng S-c, Liu Z-d, et al. The precipitation strengthening behavior of Cu-rich phase in Nb contained advanced Fe–Cr–Ni type austenitic heat resistant steel for USC power plant application. Prog Nat Sci: Mater Int 2012;22(3):175–85.
[48] Xi T, Shahzad MB, Xu D, Zhao J, Yang C, Qi M, et al. Copper precipitation behavior and mechanical properties of Cu-bearing 316L austenitic stainless steel: a comprehensive cross-correlation study. Mater Sci Eng A 2016;675:243–52.
[49] Otarola T, Hollner S, Bonnefois B, Anglada M, Coudreuse L, Mateo A. Embrittlement of a superduplex stainless steel in the range of 550–700 C. Eng Fail Anal 2005;12(6):930–41.